Drag reduction of a blunt body through reconfiguration of rear flexible plates

Cite as: Phys. Fluids **33**, 045102 (2021); https://doi.org/10.1063/5.0046437
Submitted: 03 February 2021 . Accepted: 10 March 2021 . Published Online: 01 April 2021

C. García-Baena, J. I. Jiménez-González, and C. Martínez-Bazán

Physics of Fluids ARTICLE scitation.org/journal/phf

Drag reduction of a blunt body through reconfiguration of rear flexible plates

Cite as: Phys. Fluids 33, 045102 (2021); doi: 10.1063/5.0046437
Submitted: 3 February 2021 · Accepted: 10 March 2021 ·
Published Online: 1 April 2021

C. García-Baena,[1,2] J. I. Jiménez-González,[1,2,a)] and C. Martínez-Bazán[1,2,3]

AFFILIATIONS

[1]Departamento de Ingeniería Mecánica y Minera, Universidad de Jaén, Campus de las Lagunillas, 23071 Jaén, Spain
[2]Andalusian Institute for Earth System Research, Universidad de Jaén, Campus de las Lagunillas, 23071 Jaén, Spain
[3]Departamento de Mecánica de Estructuras e Ingeniería Hidráulica, Universidad de Granada, Campus Fuentenueva s/n, 18071 Granada, Spain

[a)]Author to whom correspondence should be addressed: jignacio@ujaen.es

ABSTRACT

We investigate the quasi-static reconfiguration of rear parallel flexible plates on the drag coefficient of a blunt body. The drag coefficient, plates deformation, and main features of the turbulent wake are characterized experimentally in a towing tank. It is found that increasing the flexibility of plates leads to an important drag reduction, induced by the progressive streamlining of the trailing edge due to plates deformation. The study of the Vogel exponent is adopted here to evaluate the limit on the potential drag reduction at large values of the Cauchy number, which is shown to be mainly caused by the growth in the vibrating amplitude response of plates. The plates deformation is analyzed by means of image processing, showing that their shapes mainly follow the first modal form of a cantilever beam deflection, although a slight concavity develops toward the plates tip for large Cauchy numbers. To further analyze this process, the empirical flow loading along the plates is estimated by a modified beam theory assuming a distributed load given by a power law. The experimental fitting shows that for large flexibility, the load diminishes at the rear tip. Besides, the progressive deformation of plates is shown to weaken the shedding of vortices and reduce the size of the recirculation bubble. Finally, an affine direct relationship between recirculation bubble aspect ratio and drag coefficient has been proposed in order to quantify the linkage between near wake modifications and hydrodynamic improvement provided by the trailing edge streamlining.

I. INTRODUCTION

The flow around blunt-based bodies represents a widespread situation encountered in many engineering systems, as, for instance, heavy transport, civil structures, and marine applications. These types of flows are characterized by a massive separation at the bluff trailing edges and the subsequent development of a strong wake and a wide recirculating bubble. Such flow separation is responsible for the low base pressure and the vortex shedding. As a result, the blunt bodies have large values of drag and experience important fluctuating forces, which may entail poor aerodynamic performances or structural vibrations.

The previous considerations justify the intense work devoted to develop wake control strategies applied to blunt-based bodies[1,2] aimed to reduce the fuel consumption, increase the maneuverability of vehicles, or reduce the risk of structural fatigue induced by vibrations. In general, important reductions of the drag resistance by means of base pressure recovery can be achieved using rear systems acting on the body base or the trailing edge. That said, even though the active systems may increase the performance and optimize the drag reduction, they constitute sometimes difficult solutions to be implemented in practice and demand external energy, what may hinder their suitability in terms of global energy balance.[3] Besides, the passive devices present the advantage of its simplicity, although they do not necessarily represent optimal solutions for any flow condition.[4]

Among the passive control strategies for wakes behind blunt-based bodies, the use of base rigid cavities[5–7] delays the flow detachment and modifies efficiently the base pressure component of the drag. However, such devices do not work optimally for all flow conditions,[8] what might be partially overcome by using shape optimization techniques to design improved cavities,[9] or instead, flexible plates that may adapt better to the flow and streamline the trailing edge. In that sense, just a few recent works have studied the effect of implementing flexible parallel plates at the rear of bluff bodies with the main focus on flow-induced vibrations of the plates,[10–12] showing that a moderate

vibrating dynamics of plates may hinder the aerodynamic performance of blunt bodies in laminar regimes.

As a compromise between simplicity and capacity of adaptation to the flow, numerous attempts have been made to reproduce or develop control strategies based on biological observations (see, e.g., Refs. 13 and 14). Of particular interest are those examples of self-adaptive rigid moving flaps applied to improve the aerodynamic performance of blunt-based bodies.[15–17] In these cases, the quasi-static adaptation of flaps entails the pressure recovery at the near wake by delaying the flow separation. In a similar bio-inspired perspective, important drag reductions can be achieved by reconfiguration of flexible parts, as it occurs in plants or trees.[18,19] In particular, the observations of Vogel[20,21] demonstrated that the deformation of some parts of plants leads to lower values of drag force F_x and showed that the relationship between drag and velocity follows the scaling $F_x \propto U^{2+\gamma}$, where γ is a negative exponent. The reconfiguration of flexible structures has been extensively analyzed in applications concerning thin plates and filaments placed transversely to the flow stream,[22–28] where the reduction of the drag is associated with the streamlining of the bodies and the reduction of the exposed area. In view of these studies, the use of flexible structures, able to adapt to the flow, seems an interesting solution if a quasi-static streamlining of blunt bodies is sought.

Hence, the present analysis aims to explore the effect of the quasi-static reconfiguration of rear flexible cavities on the turbulent wake and drag coefficient of a slender blunt-based body. The role of the decreasing plates stiffness and their ability to comply with the flow will be experimentally analyzed for a fixed Reynolds number. The resulting understanding of the effect of flexibility will be useful for the design of control devices in more realistic applications, including, e.g., heavy road transport and underwater vehicles or structures. That said, this paper is organized as follows. Section II describes the problem configuration and main variables, while the experimental details and techniques are given in Sec. III. The main results and discussion are included in Sec. IV. In particular, Sec. IV A is devoted to drag force measurements. Sec. IV B presents the analysis of plates and flow forcing, while Sec. IV C describes the near wake features. Finally, the main conclusions are drawn in Sec. V.

II. PROBLEM DESCRIPTION

We study experimentally the wake behind a blunt-based body of semi-ellipsoidal nose with a total length-to-height ratio $l/h = 3.9$ and width $w = 7.64h$ (see Fig. 1). Such body, which is a slightly modified version of the model employed by Lorite-Díez *et al.*,[29] implements a rear cavity as passive control device, consisting of parallel flexible plates of length $l_c = 1.375h$ and calibrated thickness e. The plates, which are rigidly embedded at the body base, are located at an inboard distance of $h_c = 0.075h$ with respect to the rear edges. The plates width is slightly smaller than that of the body, so that a tiny gap of $0.013h$ exists between the plates and the wiglets (such intentional small gap ensures the free vibration of plates without any interference of friction with the end plates, while avoiding three-dimensional effects on the plates deformation at the plates edges).

The body is subject to an incompressible free-stream of relative streamwise velocity u_∞, density ρ_f, and viscosity μ_f, and the origin of the coordinate system (x, y) is placed at the base of the cavity hollow, and at half of the transverse height as shown in Fig. 1(b). The body is impulsively started from rest, with an acceleration rate of $a = 0.3$ m/s^2, so that the permanent regime with a constant velocity $u_\infty = u_{max} = 0.3$ m/s is reached at a time $t_p = u_{max}/a = 1$ s. The flexible plates are characterized by their density ρ_s and the Young's module E. Thus, if $I = we^3/12$ is the moment of inertia of the cross section of the plates

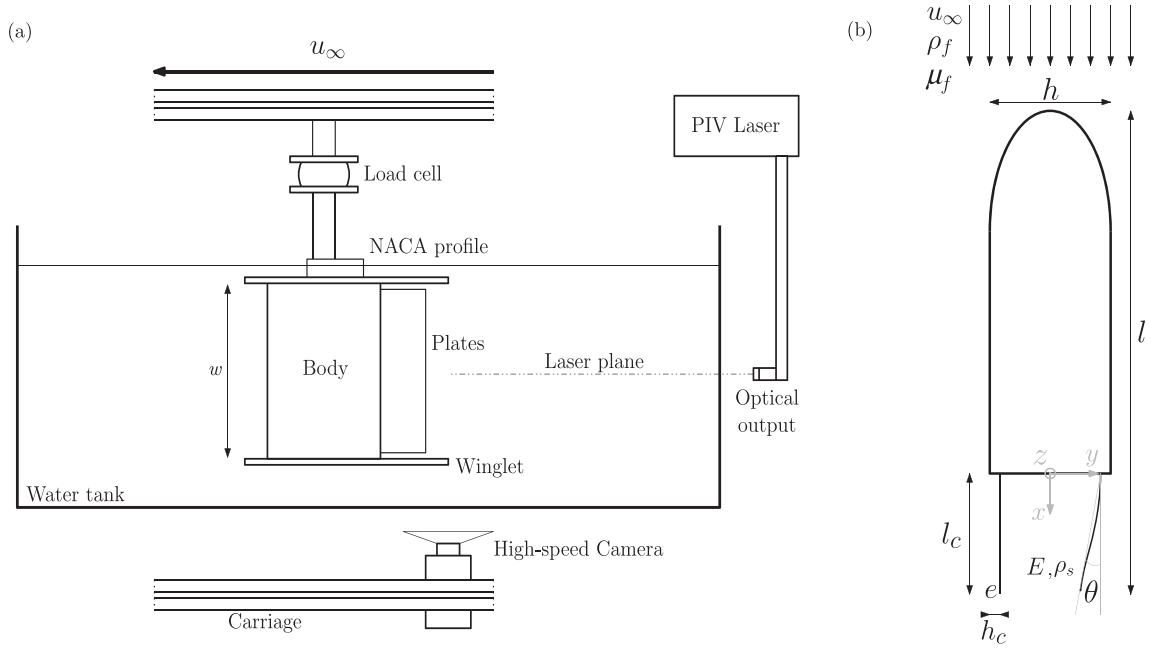

FIG. 1. (a) Sketch of the experimental setup in the towing tank and (b) problem configuration.

about the bending (z-axis in Fig. 1 pointing out of the plane), the flexural stiffness is then obtained as EI, whose value will be parametrically changed in this study by using different materials and calibrated thickness e.

That said, considering that the characteristic scales used for length, velocity, time, and pressure will be, respectively, h, u_∞, h/u_∞, and $\rho_f u_\infty^2$, the definition of the non-dimensional parameters governing the problem is given next. The Reynolds number for the permanent regime is obtained as,

$$Re = \frac{\rho_f u_{max} h}{\mu_f}, \tag{1}$$

whose value will be kept constant for the present study at $Re = 12\,000$. Besides, the non-dimensional stiffness of the plates under the flow action can be quantified through the Cauchy number,[23]

$$Ca = \frac{\rho_f u_{max}^2 l_c^3}{2EI}, \tag{2}$$

which represents the ratio of the force produced by the characteristic dynamic pressure of the flow and the bending stiffness of the flexible plates. The modification of the plates' material and calibrated thickness, e, allows to modify the flexural stiffness EI, thus covering the range of Cauchy numbers $0.006 \leq Ca \leq 56.221$ for the present study, as listed in Table I, where the main characteristics of the different flexible plates are summarized. Moreover, the variation of the plates flexural stiffness can be also accounted for through their reduced velocity,

$$U^* = \frac{u_\infty}{\varpi_{1,n} h}, \tag{3}$$

where $\varpi_{1,n}$ represents the natural linear frequency of the flexible plates corresponding to the first mode of vibration. In particular, the value of $\varpi_{1,n}$ is estimated using the Euler-Bernoulli beam theory, and modeling the plate vibration as a free vibration of a cantilever beam.[30] More precisely, the natural linear frequencies of the different k-th modes of vibrations or eigenmodes can be then computed as,

$$\varpi_{k,n} = \frac{(\beta_n l_c)^2}{2\pi} \sqrt{\frac{EI}{\rho_s e w l_c^4}}, \tag{4}$$

where β_n is a dimensionless coefficient, which solves the frequency equation $\cos(\beta_n l_c) \times \cosh(\beta_n l_c) = 1$. The solution involves infinite roots, with the smallest one occurring somewhere past the point where the cosine function first becomes negative. Thus, it is demonstrated that $\beta_1 l_c = 1.8751$ is the constant of the natural frequency for the first mode of free vibration of a cantilever beam, with l_c being the beam length and β_1 the coefficient of the first normal mode. As listed in Table I, the present study covers the range of reduced velocity $U^* = [0.077, 1.552]$. Note that $U^* = 0$ would correspond to a perfectly rigid case (case #1 will be used here as a rigid reference configuration). Additionally, a solid-to-fluid mass ratio $m^* = \rho_s/\rho_f$ can be defined, although the two materials employed in the study provide with similar values, i.e., 8.4 and 7.9 for brass and steel, respectively, and therefore, little effect is expected on the results.

TABLE I. Main features of flexible plates investigated.

Foil #	Material	e (mm)	E (MPa)	Ca	$f_{n,1}$ (Hz)	U^*
1	Brass	0.5	1.1×10^5	0.006	96.61	0.077
2	Brass	0.2	1.1×10^5	0.102	38.65	0.194
3	Brass	0.15	1.1×10^5	0.242	28.98	0.259
4	Brass	0.1	1.1×10^5	0.817	19.32	0.388
5	Brass	0.075	1.1×10^5	1.936	14.49	0.517
6	Steel	0.05	2.1×10^5	3.422	13.81	0.543
7	Brass	0.05	1.1×10^5	6.533	9.66	0.776
8	Steel	0.025	2.1×10^5	27.375	6.90	1.086
9	Brass	0.025	1.1×10^5	56.221	4.83	1.552

The plates instantaneous deformation obtained for each value of Ca can be quantified through the inclination angle of the fitted chord line θ, measured with respect to the streamwise direction, as depicted in Fig. 1(b). Besides, the effect of the plates deformation will be analyzed in terms of force coefficients and characteristic frequencies. For instance, the drag coefficient will be obtained as,

$$c_x(t) = \frac{\mathrm{f}_x(t)}{0.5\rho_f u_{max}^2 h w}, \tag{5}$$

where $\mathrm{f}_x(t)$ denotes the time-dependent drag force (i.e., in the streamwise direction). In addition, characteristic frequencies of the time evolutions of the flow variables, ϖ, will be presented in dimensionless form as Strouhal numbers,

$$f = \frac{\varpi h}{u_{max}}, \tag{6}$$

where the dominant frequencies will be calculated from the Fourier transform of the corresponding time series. Any frequency can be also presented in non-dimensional form by normalizing it by the natural frequency of the first mode of vibration of the plates, as

$$f^* = \frac{\varpi}{\varpi_{1,n}}. \tag{7}$$

In the following, all the variables will be given in dimensionless form, unless otherwise stated. Besides, the time-dependent variables will be denoted using lower case variables, $\psi(t)$, while their temporal averaged will be expressed by capital ones, $\Psi = \bar{\psi}$. Additionally, the instantaneous amplitude of any fluctuating variable $\psi'(t) = \psi(t) - \Psi$, denoted as $\hat{\psi}$, will be obtained by means of the Hilbert transform (with $\mathcal{H}$ denoting the operator). In particular, to form the analytic signal on the complex plane,[31] whose real and imaginary components are, respectively, $z_r = \psi$ and $z_i = \mathcal{H}(\psi)$. Therefore, the instantaneous amplitude (envelope) and phase in the complex plane can be obtained as $\hat{\psi} = \sqrt{z_r^2 + z_i^2}$ and $\psi_\psi = \arctan(z_i/z_r)$, respectively, so that the corresponding time-averaged amplitude is expressed as $\hat{\Psi} = \overline{\hat{\psi}}$.

III. EXPERIMENTAL DETAILS AND TECHNIQUES

A. Setup configuration

The experiments were carried out in a towing tank of 2 m × 0.6 m × 0.6 m, which allows optical access from all sides. The body was towed and controlled through an Adjustable Frequency Drive (AFD) connected to an AC motor that provided a stable linear displacement for velocities up to 0.66 m/s. The control of the velocity and the

acceleration by the AFD provided sensitivities of 70 μm/s and 80 μm/s^2, respectively. The towing facility was systematically calibrated to ensure a correct determination of the velocity and repeatability of the flow conditions, leading to uncertainties in the value of u_{max} of ± 0.005 m/s.

The body, manufactured using a 3D printer, was connected to the towing carriage using a steel shaft holding from a turntable platform, which allowed a precise alignment of the body with respect to the incident stream. The lower end of the shaft featured an external casing with a streamlined 1 cm thick NACA profile shape to avoid the massive flow separation close to the free surface. A load cell was installed between the platform and the body to account for the drag force measurement, as shown in Fig. 1(b). In addition, two thin acrylic plates of 3 mm thickness (chamfered at their front) were placed at the body ends close to the free surface and ground, to avoid any effect of the free surface waves and ground clearance. It should be noted that the frontal submerged area offered by end plates and the holding device represents only a 5.86% of the total body's area, and therefore, their contribution to the drag coefficient can be considered marginal for such a comparative study. Blockage effects can be estimated from the ratio between the spanwise height of the body $h = 4$ cm and the width of the channel, $w_c = 60$ cm, providing $h/w_c = 0.067$ (6.7%) which leads to a velocity variation of $\Delta u/u = 0.71$ (7.1%). With this velocity correction, the drag coefficient correction should give $\Delta C_x/C_x = 0.13$ (about 13% lower). However, the data presented in this work have not been blockage corrected since it is a comparative study where the measurements reported were taken under the same conditions, i.e., with a constant blockage. Besides, the rear flexible cavity was installed at the body base using an add-on system that allowed to rigidly hold the calibrated metallic foils, by means of adjustable slits guided by holding screws. As a result, the flexible plates were located at an inboard distance of $h_c = 0.075h$ with respect to the rear edges (Fig. 1).

B. Force and frequency measurements

The drag force was measured using a force sensor (model AMTI-MC3A-100lb), connected to the moving carriage through a rigid support. The accuracy of the load cell was estimated to be of ± 0.001 N (using specifications of hysteresis, crosstalk, and non-linearity). The data were acquired at a sampling rate of 1 kHz, performing a number of runs of $n = 6$ with each plate to ensure a good repeatability of the results.

On the other hand, the characteristic shedding frequency at the wake was obtained for all cases from transverse velocity $u_y(t)$ measurements, performed with a one-dimensional, 658 nm, miniature LDV system (model MSE miniLDV^{TM}), whose probe volume was $30 \times 60 \times 200\ \mu$m^3. To that end, the flow was seeded with 10 μm neutrally buoyant hollow glass spheres. The probe was located at a downstream distance of $x = 3h$, where the amplitude of velocity fluctuations was proven to be sufficiently energetic for the analysis. Thus, using proper decimation, threshold and SNR values, approximately 5000 particles, were registered for each run, what, considering a run temporal length of 6s, provided with an equivalent, equi-spaced temporal resolution of $\Delta t \sim 0.001$ approximately. The transverse velocity data were subsequently processed and fitted, to perform a spectral analysis of the time-series $u'_y(t) = u_y(t) - U_y$, to obtain the main frequencies at the wake. Note that such frequencies are of order of 2–3 Hz, far below the natural frequencies of the body-holding system, which were checked to be above 15 Hz.

Furthermore, additional force and frequency measurements were also performed in a water tunnel facility with a test section of 0.4 m $\times$ 0.4 m $\times$ 2.5 m. These additional measurements allowed to satisfactorily verify that the force and frequency values obtained at the towing tank corresponded to permanent flow regime conditions. In fact, the comparison between measurements from the towing tank and the water channel was estimated to be lower than 5% both for time-averaged drag force and main frequency results.

C. Particle image velocimetry

Wake visualizations of the xy plane were carried out at the towing tank using time resolved, planar Particle Image Velocimetry (PIV). To that aim, a 5 W Diode-Pumped Solid State (DPSS) green laser with a 50 mm cylindrical lens was used to create a horizontal sheet at $z = 0$, illuminating from behind the body, as depicted in Fig. 1(a). As mentioned earlier, the flow was seeded with 10 μm, neutrally buoyant hollow glass spheres. The images were acquired with a CCD-sensor, 12 bit, 1 Mpixel High-Speed Camera equipped with 60 mm f/2.8 fixed focal lens objective. The camera was located at the bottom of the carriage and towed alongside the body [see Fig. 1(a)]. This setup provided with an approximate Field of View (FoV) of $3h \times 2h$ behind the body, which allowed to properly capture the recirculation region and the vortex shedding. The images were recorded with a resolution of 1024×1024 pixels and an acquisition rate of 1000 fps, with a time interval $\Delta t = 2$ ms after PIV processing. Moreover, the shutter speed was accordingly adjusted to a value of 1/2000 s, to obtain static particles between consecutive snapshots.

Using the previous settings, series of around 2000 pair of images were processed in each experimental case, using the MATLAB® toolbox PIVlab.[32] As an initial step, a mask was applied to all images, in order to exclude the body base and the region of plates displacement out of the analysis. Subsequently, a pre-processing was done to all the images to increase the contrast and brightness of points between images, after what a Fast Fourier Transform (FFT) cross correlation algorithm was applied. In particular, to account for the differences of velocity in the region of interest, three distinct consecutive interrogation windows with respective sizes of 64×64, 32×32, and 16×16 pixels were used in combination with a 50% overlapping area. As a result, a vector field of 124×62 and a spatial resolution of $0.034h$ were obtained, with the number of spurious vectors obtained being very small and always less than 2% of the total.

The temporal and spatial uncertainties of the estimated magnitudes from the PIV measurements of velocity can be obtained from Taylor series propagation,[33] considering Δx and Δt as independent variables,

$$\left(\frac{U_u}{u}\right)^2 = \left(\frac{U_{\Delta x}}{\Delta x}\right)^2 + \left(\frac{U_{\Delta t}}{\Delta t}\right)^2. \tag{8}$$

The uncertainty in the time separation, $U_{\Delta t}$, in our case relies upon information provided by the manufacturer of the high-speed camera. Typical values of $U_{\Delta t}$ are of the order of 1 ns, yielding a negligible relative uncertainty in our case. With respect to $U_{\Delta x}$, a great amount of work has been developed to quantify uncertainties in PIV

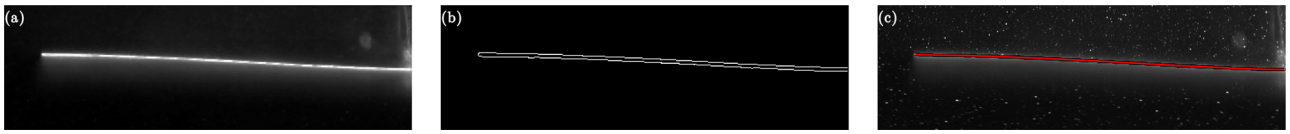

FIG. 2. Example of the different stages in the plate deformation detection algorithm corresponding to a random instant and plates configuration #7 in Table I: (a) pre-processed image without background noise, (b) image with edge detection after application of the homogeneity operator, and (c) cubic spline fitting (red line) together with the original raw image (background).

measurements.[34] However, a rough estimation can be given by cd_p, being d_p the particle image diameter and $c \sim 0.1$ a parameter associated with the uncertainty in locating the particle image centroid.[35] Typical values of minimum measurement errors have been reported in the range of 0.05–0.1 pixels for 32×32 pixels interrogation window. Thus, in our PIV measurements, it is expected to have uncertainties lower than 1%. A similar derivation can be also used to estimate the uncertainty for frequency, or plates deformation obtained from visualizations as described below.

D. Plates deformation characterization

To characterize the plates displacement, a similar image acquisition procedure with the help of the high-speed camera was applied to the region of interest of the plates. Thus, the light reflection created by the metallic shining surface of plates due to the incidence of the horizontal laser sheet was captured by the camera (to enhance the shinning, the plates were covered by a solution with hollow glass particles). The 12 bits gray-scale raw images, acquired with a resolution of 1024×1024 pixels and a sampling rate of 1000 fps, were processed with the help of the MATLAB® image processing toolbox, where a series of filters were applied in order to improve the shape detecting algorithm. In particular, a Gaussian filter was applied to the cropped images to remove any particles from the flow [see Fig. 2(a)], and the edges of the plate were subsequently detected applying a homogeneity operator. The threshold for binarization was calculated applying the Otsu's method, using the value 1 for the pixels at the plate's edge [see Fig. 2(b)]. Additionally, to clear the image and reduce the remaining noise, all the images were processed creating a weight matrix adding all the pixels with values 1 from the different frames, thus obtaining a spatial heat map around the area of the plate locations. Thanks to the relatively small displacement of the plate, a well-defined area was observed, what also helped to eliminate noise or particles. After that, a second processing iteration was performed, where a geometric weighed mean was computed for each column of the image to define a line that represented the shape of the plate corresponding to each snapshot. These points were finally fitted by a cubic spline interpolation, applying the extra contour condition of a nil second derivative at the embedding on the body base [see Fig. 2(c)].

IV. RESULTS AND DISCUSSION

A. Drag force

Figure 3 shows a typical time-evolution of the drag force $c_x(t)$ for the bluff body with rear flexible plates. Due to the initially accelerated motion from rest and the final deceleration of the carriage, the drag force $c_x(t)$ displays an initial added mass positive peak and a negative peak at the end of the run. The value of $c_x(t)$ corresponding to the steady regime of the body can be then obtained after discarding the accelerating and decelerating transients. The limits of the analysis window are illustrated in Fig. 3, where t_i and t_f denote, respectively, the initial and final times. Considering that the acceleration time taken by the body to reach the steady regime was set to 1 s for all cases, a safe value of $t_i \simeq 1.35$ s is defined. The suitability of such value t_i to provide statistical convergence of the standard deviation of the drag, considering moving temporal windows of 0.3 s, has been also satisfactorily tested. Finally, the value of t_f is set after the detection of the deceleration peak to obtain the windows of analysis with a length of $\Delta t = 4$ s.

It still remains unanswered whether the run length is sufficient long to obtain permanent regime values of the forces. In that sense, according to the definition given by Fernando and Rival,[36] the non-dimensional run distance corresponding to the permanent motion of the carriage is $s/D_h \simeq 21$, where $D_h = 2hw/(h+w)$ is the hydraulic diameter of the body's section. After comparing this value to those reported in previous studies on impulsively started bluff devices,[36,37] such distance can be considered long enough to provide steady drag values. Moreover, to discard any transient effect on the results, additional measurements of forces were performed in the water channel facility for selected values of the Cauchy number, obtaining differences always below 5% for the time-averaged drag C_x in all cases analyzed.

After the definition of the analysis windows for the steady regime, the characteristic time-averaged drag C_x and the mean amplitude of the drag fluctuations $c'_x(t)$, i.e., $\hat{C}_x$, are computed. The mean values, C_x and $\hat{C}_x$, obtained from the different $n = 6$ tests corresponding to each Cauchy number (i.e., $\frac{1}{n}\sum_{i=1}^{n=6} C_{x,i}$ and $\frac{1}{n}\sum_{i=1}^{n=6} \hat{C}_{x,i}$) are depicted in Fig. 4(a), while the corresponding relative variations with respect to

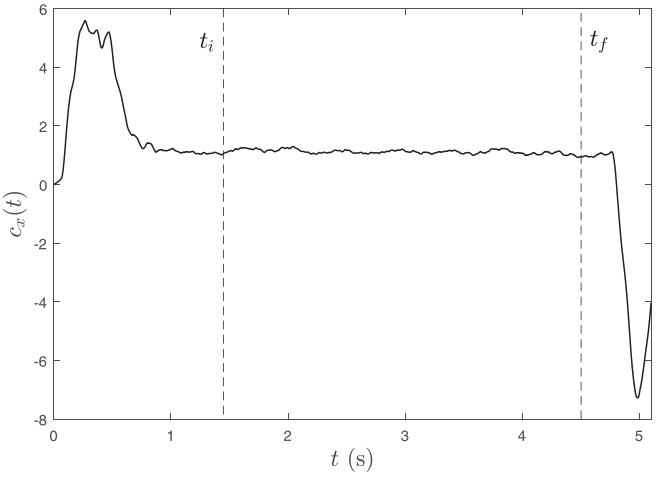

FIG. 3. Example of drag coefficient measurements for a Cauchy number of $Ca = 0.06$, i.e., case #1, and analysis window for the steady drag analysis inscribed between initial and final instants, t_i and t_f (see thin-dashed vertical lines).

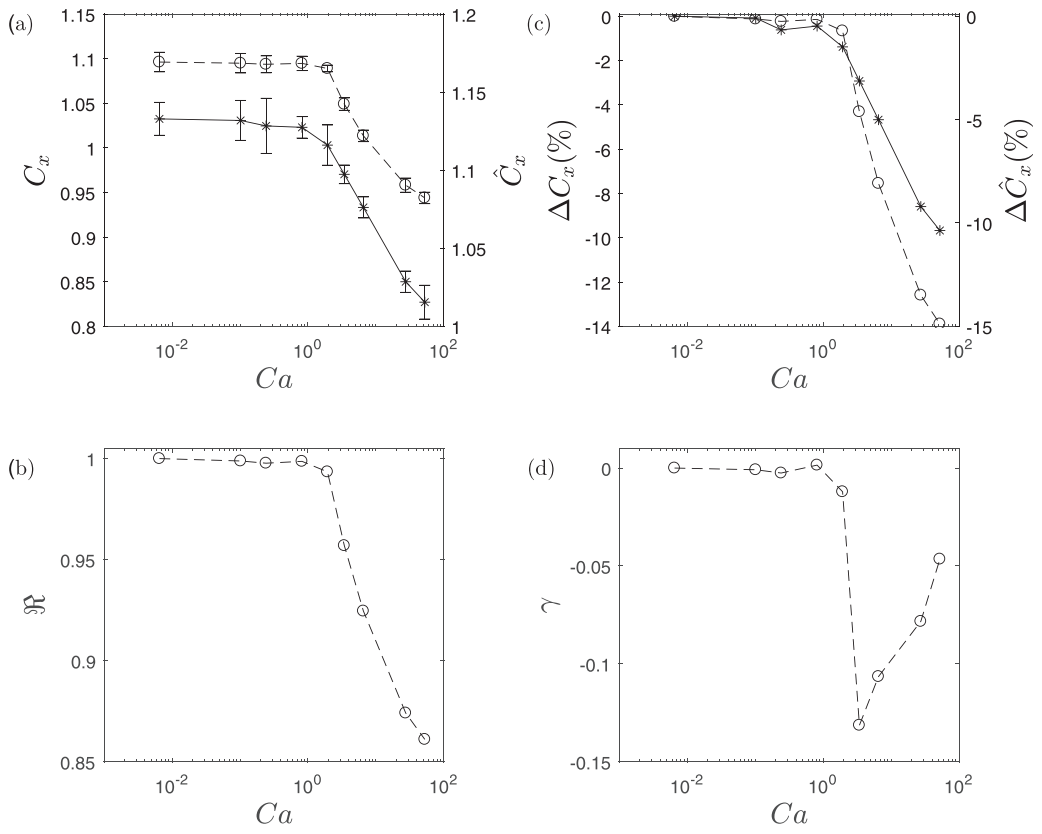

FIG. 4. Evolution with the Cauchy number Ca of (a) time-averaged drag coefficient, C_x (dots), and magnitude of drag fluctuations, $\hat{C}_x$ (asterisks), and (b) corresponding relative variations with respect to the rigid case, ΔC_x and $\Delta \hat{C}_x$; (c) reconfiguration number $\Re = C_{x,i}/C_{x,0}$; and (d) Vogel exponent $\gamma = 2\partial \ln \Re / \partial \ln Ca$. Error bars in (a) show the respective standard deviation of results for C_x and $\hat{C}_x$, and $\sigma(C_x)$ and $\sigma(\hat{C}_x)$, obtained from the different $n = 6$ runs.

the rigid reference case (#1 in Table I) are included in Fig. 4(b). Note that the variability of results in (a) is shown by means of error bars that quantify the standard deviation of the measured values from the different $n = 6$ runs, i.e., $\sigma(a) = \sqrt{\frac{1}{n-1}\sum_{i=1}^{6} |a_i - (\frac{1}{n}\sum_{i=1}^{n=6} a)|^2}$, where a_i is the values of C_x or $\hat{C}_x$ for each run.

As observed, the drag coefficient for the stiffest case of $Ca = 0.006$ is $C_x = 1.099$, which, in the following, will be considered the rigid reference value $C_{x,0}$. As the Cauchy number increases, the drag decreases very slowly initially, but there is a sudden reduction for $Ca \geq 1.936$, presumably due to the deformation of the plates to adapt to the flow streamlines, reaching a value of 0.944 for the most flexible case with $Ca = 56.221$. Note that, a similar trend is observed for the amplitude of drag fluctuations, $\hat{C}_x$, due to that the more streamlined trailing edge leads to a weakened shedding process at the wake. The corresponding maximum variations of the time-averaged drag ΔC_x and magnitude of drag fluctuations $\Delta \hat{C}_x$ are, respectively, 13.9% and 10.4%, for the largest value of Ca, as shown in Fig. 4(b).

The decrease in the drag force induced by the plates reconfiguration can be also indirectly quantified by means of the so-called Vogel exponent.[20] In particular, the classical quadratic velocity-drag law at large Re for rigid bodies $F_x \propto U_\infty^2$ is modified to a smaller power law $F_x \propto U_\infty^{2+\gamma}$, where γ is the Vogel exponent (typically negative values of 0 and -1 indicate, respectively, quadratic and linear relationships between velocity and drag). As highlighted above, the computation of γ has been traditionally employed in problems concerning flexible filaments or plates placed transversely to the flow stream, to evaluate the effective front area reduction and the streamlining of the body for different shearing flows [see, e.g., Refs. 22, 23, and 38–40]. Thus, although the present configuration is not rigorously equivalent in terms of the fluid-structure interaction (the incident flow is parallel to the plates), such exponent can be useful to establish similarities and to evaluate the capability of the flexible plates to comply with the flow, or even to determine the existence of a limit in the progressive decrease in drag force with the Cauchy number. That said, the Vogel exponent can be computed as

$$\gamma = 2\frac{\partial \ln \Re}{\partial \ln Ca}, \tag{9}$$

where $\Re = C_x/C_{x,0}$ is the reconfiguration number.

The evolutions of $\Re$ and γ with the Cauchy number Ca are depicted in Figs. 4(c) and 4(d), respectively. Evidently, the trend of $\Re$ is the same as that of ΔC_x, displaying a strong decrease at large Ca. The modification of the slope in the logarithmic scale is given by the Vogel exponent, which displays negative values for $Ca \geq 1.936$, from

where the quadratic law $F_x \propto U_\infty^2$ no longer holds. In particular, the exponent displays a minimum value of –0.131 at $Ca = 3.422$, to subsequently increase and reach a value of -0.047 for the most flexible case investigated. This trend is qualitatively similar to those reported for reconfiguration processes of flexible plates placed transversely to the flow (see e.g., Ref. 23), and it is likely that for larger values of Ca, an asymptotic limit might be found, meaning that there is a limit on the potential decrease in the drag force with the increase in flexibility. However, it is evident that the present configuration, where the incident flow is initially parallel to the plate, is structurally different from that of Gosselin *et al.*,[23] and no further analogies can be established with respect to previous works (a deeper analysis, including, for instance, the effect of the transverse velocity profile at the trailing edge, is beyond the scope of the present study). Nevertheless, after identifying a possible limit on the drag reconfiguration at large Ca, we will next analyze the plates deformation process to identify the underlying mechanisms behind the force results.

B. Analysis of the plates deformation

The effect of the Cauchy number on the plates dynamic response will be next discussed. To that aim, the deformation of the different flexible plates has been analyzed by means of image processing, as described in Sec. III. The time-averaged shapes of the plates for the four selected representative values of the Cauchy number, i.e., $Ca = 0.817, 1.936, 6.533,$ and 56.221 (corresponding to cases #4, #5, #7, and #9 in Table I, respectively), are depicted in Fig. 5. These cases will be considered to illustrate the results, since they are representative of negligible, small, intermediate, and large relative reductions of the mean drag coefficient and the amplitude of the drag fluctuations in Fig. 4. As expected, the mean deflection of the cavity plates (thick solid lines) increases with Ca, giving rise to a more streamlined configuration of the bluff bodies for the less rigid cases. Thus, the decrease in the drag coefficient reported in Sec. IV A can be, therefore, attributed to a smooth reconfiguration process of the plates, which modifies the flow detachment at the rear edges and reduces the bluffness of the near wake, as it will be shown below.

Another remarkable feature of the plates deflection is the existence of a slight concavity upward close to the plates tip for larger values of the Cauchy number. Such behavior for highly flexible foils may be induced by the decrease in the inward transverse fluid load occurring near the tip, on the account of the shear layer detachment at the rear edges. Such issue will be, however, addressed more in detail below. Interestingly, the deformed shape for low stiffness in Fig. 5(d) resembles the curved profile obtained by Lorite-Díez *et al.*[9,29] using shape optimization techniques. They showed that the use of a curved cavity profile efficiently reduces the drag coefficient, when compared to the classical device of rigid straight cavity, due to an induced inward flow deflection, that reduces the wake extend and rises the base pressure.

The inclination angle, θ, of the chord line (the straight line connecting the tip and root of the plates), defined with respect to the horizontal direction [see Fig. 1(b)], is a good quantitative estimation of the general plates deformation. In order to analyze, respectively, the quasi-static plates reconfiguration and the response dynamics, we depict in Fig. 6 the time-averaged chord angle, Θ [Fig. 6(a)], and the amplitude of the angle fluctuation, $\hat{\Theta}$ [Fig. 6(b)], for selected values of the Cauchy number. As observed, the mean deformation of the plates given by Θ increases monotonously with Ca, although three different trends are observed. At low values of the Cauchy number, $Ca \leq 0.816$ (high values of the bending rigidity), the deformation is very small and grows very slowly with increasing Ca. This range is associated with negligible reductions of the drag coefficient, as observed in Fig. 4. At intermediate values of the Cauchy number ($0.816 < Ca \leq 27.375$), the mean angle grows at a considerable rate, indicating a strong reconfiguration of the cavity plates that lead to a rapid relative drag reduction observed for such range in Fig. 4(a). Finally, at high values of Ca (> 27.375), the rate of growth of the mean angle is seen to decrease, inducing the increase in the Vogel exponent at large values of Ca observed in Fig. 4(d).

On the other hand, the influence of the plates stiffness on the dynamic behavior is analyzed next with the help of Fig. 6(b), where the amplitude of the chord angle fluctuations is plotted against the Cauchy number. As observed, the amplitude of plates angular

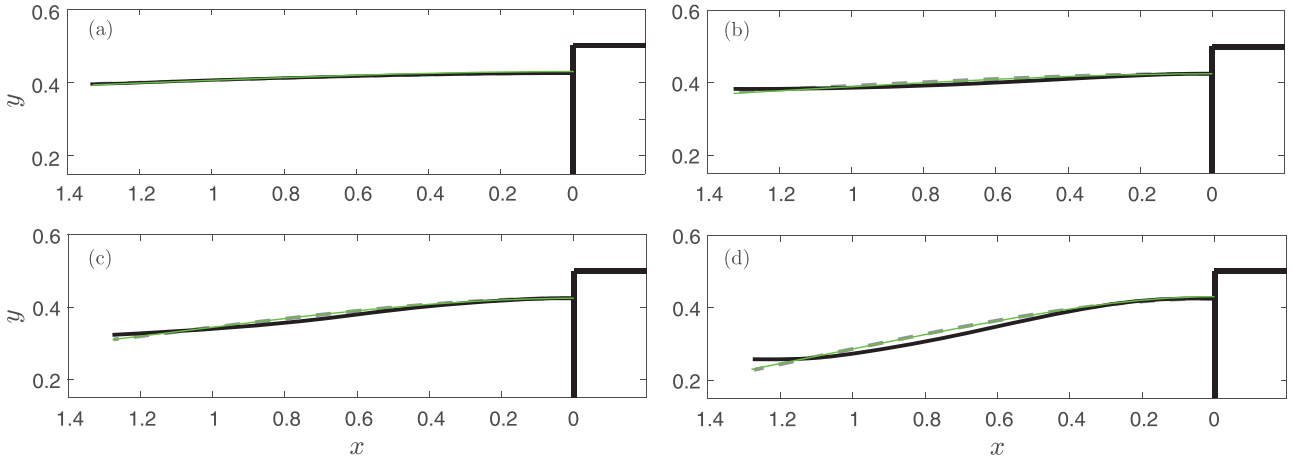

FIG. 5. Mean deflection of flexible plates for the selected values of Cauchy number (see Table I) (a) #4 $Ca = 0.817$, (b) #5 $Ca = 1.936$, (c) #7 $Ca = 6.533$, and (d) #9 $Ca = 56.221$: experimental deflection obtained from image processing (thick solid black lines); approximate shape of the first Euler–Bernoulli mode of free vibration (dashed gray line); and estimate of static deflection according to the theoretical Euler–Bernoulli theory with varying distributing load (thin solid green line).

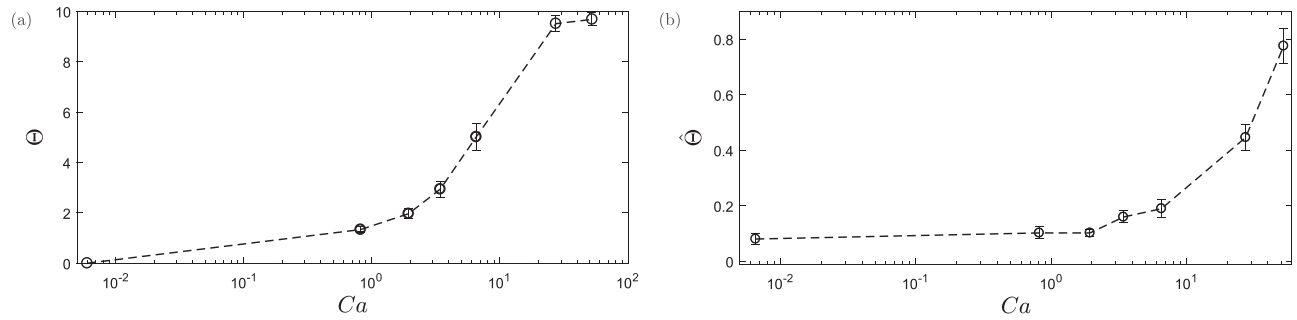

FIG. 6. Mean deflection angle Θ and amplitude of oscillations $\hat{\Theta}$. Error bars show the respective standard deviation of results, $\sigma(\Theta)$ and $\sigma(\hat{\Theta})$, obtained from the different $n = 6$ runs.

oscillations $\hat{\Theta}$ is negligible for $Ca < 3.422$, with values close to 0.1°. The slight mean deformation and the weak amplitude dynamic response of the plates suggest that they are too stiff to response to the flow forcing. Thus, the small limit of $\hat{\Theta} \simeq 0.1°$ for the stiffest cases can be attributed to be the magnitude of the structural vibrations of the experimental setup of a body and holding system, which can be considered negligible (note that the image processing procedure detailed in Sec. III provides a spatial resolution of 0.04 mm, while the transverse displacement of the plate's tip for the minimum angle of $\hat{\Theta} \simeq 0.1°$ is approximately 0.1 mm given the plate's length). Besides, a sudden increase in the angular oscillations takes place for higher values of the Cauchy number, i.e., $Ca \geq 6.533$, indicating the beginning of a regular flow-induced vibrations regime. The maximum amplitude of the angular oscillations for the highest value of Ca under study is found to be $\hat{\Theta} \simeq 0.8°$, what remains small enough to consider the general response of the plates as quasi-static. However, the oscillations at $Ca = 52.261$ seem to hinder the growth with decreasing stiffness of the mean deformation as observed in Fig. 6(a), what may represent a practical limit in terms of drag reduction and justifies the selection of the range of Cauchy number for the present study.

To complement the analysis of the rear cavity response and approximate coupled dynamics, the deformation of the plates has been also compared to the shape of the first Euler-Bernoulli mode of free vibration. In particular, the equation of deflection for the first normal mode reads[30]

$$y_{1,n} = A\,[\sin\beta_1 x - \sinh\beta_1 x - \alpha_n(\cos\beta_1 x - \cosh\beta_1 x)], \qquad (10)$$

with $\alpha_n = (\sin\beta_1 l_c + \sinh\beta_1 l_c)/(\cos\beta_1 l_c + \cosh\beta_1 l_c)$ and $\beta_1 l_c = 1.8751$. The amplitude A has been adjusted for each case under study using a least squares approximation, to give the plates deflection represented in Fig. 5 by thick-dashed lines. As observed there, the shapes of the normal modes seem to capture properly the plate deformation, although for larger values of the Cauchy number, the reported concavity upward close to the tip deviates the foil profile from the theoretical normal mode estimation. Nevertheless, to identify whether such concavity is associated with any vibration of the plates caused by secondary Euler–Bernoulli modes, a proper orthogonal decomposition (POD) has been performed to snapshots of the plates deformation (see García-Baena *et al.* for details[12]). In that sense, the dominant (and coherent) POD mode shape, containing nearly 95% of the vibration energy, is remarkably close to the first Euler-Bernoulli mode deflection, thus discarding the concurrence of a secondary vibration mode.

The frequency response of the plates has been also analyzed with the image processing procedure described above. In particular, at least 2000 frames corresponding to the permanent regime (identified in Fig. 3) have been processed, covering a minimum time interval of 2 s, what means that approximately 5 vibration cycles have been captured for the slowest plates dynamics. The frequency ratios defined with respect to the first natural frequency of vibration, $f_{n,1}$ (see Table I), and given by the main characteristic frequencies of the plates vibration, $f_p^* = f_p/f_{n,1}$, are depicted in Fig. 7 for selected values of the Cauchy number. As observed, f_p^* grows linearly with U^* (i.e., monotonously with Ca), although they lie below $f^* = 1$ for the whole range of U^* investigated, meaning that the plates oscillate with a frequency lower than their corresponding natural frequencies of vibration. Additionally, the characteristic frequency ratios of the wake vortex shedding $f_w^* = f_w/f_{n,1}$, obtained for each U^* (by means of the LDV measurements taken at $x = 3$), have been included in Fig. 7 (asterisks) for comparison, along with the Strouhal linear law given by the vortex shedding behind the rigid case, i.e., $f^* = St_w^r\, U^* = 0.26\, U^*$. The dominant shedding frequency ratio is seen to coincide with that of the plates vibration, indicating that the wake dynamics governs the frequency response of the plate. Interestingly, the values of f_w^* are above the linear law given by the Strouhal number of the rigid cavity, taken to be that at $Ca = 0.006$. This observation indicates that the resulting shedding frequency f_w grows with U^* (or Ca), i.e., as the plates mean deformation becomes larger. Thus, as the distance between rear plates edges decreases, the interaction between the closer shear layers is fostered and the shedding process accelerates. Besides, this frequency response characterized by $f^* < 1$ and governed by the vortex shedding dynamics is a typical scenario in vortex-induced vibration problems at low values of the reduced velocity (see, e.g., Ref. 12). In particular, if U^* is increased above 2, it is expected that the frequency ratio reaches eventually $f^* \simeq 1$, what would define the beginning of the synchronization, surely leading to enhanced vibrations of large amplitude. Therefore, the mitigated amplitude response of vibrations observed in Fig. 6(b), even for the largest value of $Ca = 55.26$, is the result of the range of low values of U^* explored in the present study.

In view of the weak dynamic amplitude response of the plates, we next perform a quasi-static analysis to estimate, theoretically, the time-average foil deflection and the flow loading distribution giving rise to the plates deformations illustrated in Fig. 5. To that aim, the same linear Euler-Bernoulli beam theory approach used by Sathessh and Huera-Huarte[40] to quantify the deflection of flexible foils being towed

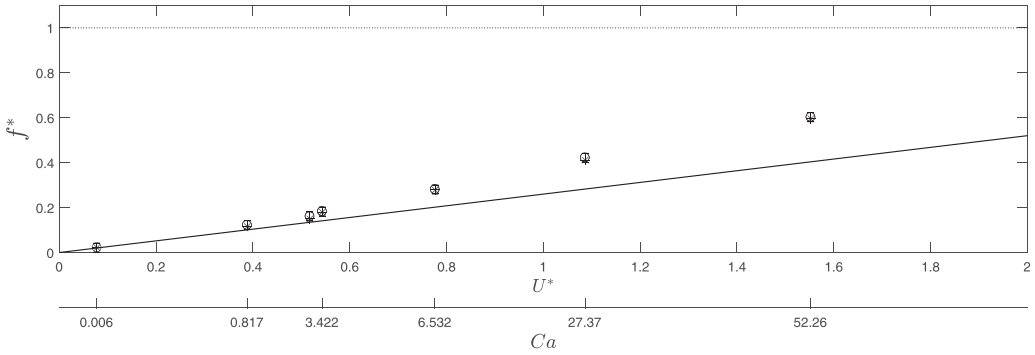

FIG. 7. Main characteristic frequency ratios of plates vibration $f_p^* = f_p/f_{n,1}$ (open circles) and wake vortex shedding $f_w^* = f_w/f_{n,1}$ (asterisks), as a function of the reduced velocity U^* and Cauchy number Ca. The solid line represents the Strouhal law vs U^* given by the reference rigid cavity body $f^* = St_w^r \cdot U^*$, with $St_w^r = 0.26$. Error bars show the standard deviation of results $\sigma(f^*)$ obtained from the different $n = 6$ runs.

normal to the flow will be employed here. In particular, the transverse deflection y for a cantilever uniform beam is given by $EI\partial^4 y/\partial x^4 = q$, where q is the applied load (see e.g., Ref. 41). Thus, for the present analysis where the flow loading is unknown, we can assume that the plate is subject to a distributed load that varies along the span with the form $q = q_0(1 - x/l_c)^n$, where n is the loading exponent. Therefore, $n = 0$ represents a uniformly distributed load with a constant value q_0, and $n = 1$ gives a uniformly varying load, with nil and maximum force attained, respectively, at $x = l_c$ and $x = 0$. Substituting the loading expression into the beam equation, one obtains

$$EI\frac{\partial^4 y}{\partial x^4} = q_0\left(1 - \frac{x}{l_c}\right)^n, \tag{11}$$

that can be integrated with the proper boundary conditions to yield,

$$y = \frac{q_0 l_c^4}{EI(n+1)(n+2)(n+3)(n+4)} \times \left[\left(1 - \frac{x}{l_c}\right)^{n+4} - \left(1 - \frac{x}{l_c}\right)(n+4) + (n+3)\right]. \tag{12}$$

Equation (12) has been used to obtain the load exponent, i.e., the flow loading distribution estimation, by fitting the experimental data of the four cases represented in Fig. 5, where the corresponding fits are also depicted (see thin green lines). As expected, the theoretical static estimation of the linear deflection is nearly identical to the shape of vibration modes. The approximate exponents leading to the fits of $Ca = 0.816$, 1.936, 6.533, and 52.261 are, respectively, $n = -0.5$, -0, 4, -0.22, and 0.8. The resulting load distributions q/q_0 are plotted in Fig. 8, where it can be observed that for $Ca = 0.816$, 1.936, and 6.533, the flow loading increases toward the plate rear tip since the exponent is negative, while it decreases toward the tip for $Ca = 52.261$, which features a positive exponent. Thus, it is shown that the plate concavity upward develops for low stiffness cases, as the loading at the rear tip drops with increasing Ca. The modifications on the flow separation inducing such estimated loading change will be subsequently analyzed using PIV measurements.

C. Near wake visualizations

To evaluate the wake topology modifications induced by the plates deformations, we conducted several PIV measurements for selected values of the Cauchy numbers. First, the spanwise vorticity distributions were computed from the measured velocity fields and made dimensionless using the free-stream velocity and the body's height. Thus, Fig. 9 displays the time-sequence of half of a shedding cycle through snapshots of the instantaneous vorticity contours, $\omega_z(x, y)$, and streamlines, for $Ca = 1.936$, 6.533, and 56.221 corresponding to cases of small, intermediate, and large plates deformation (see Fig. 6), respectively. The shedding sequence in these cases is described as follows. At $\phi = 0$, a clockwise vortex developed at the lower plate grows and covers most of the near wake, as the flow detaches from the lower shear layer. Subsequently, a counterclockwise vortex starts to form at the edge of the upper plate ($\phi = \pi/4$) and interacts with the lower one. The upper vortex growth precludes the lower one to penetrate inside the cavity ($\phi = \pi/2$), which is advected downstream from the body as the upper vortex shifts toward the axis ($\phi = 3\pi/4$). Thus, the counterclockwise vortex covers most of the near wake in $\phi = \pi$, from which a new shedding process begins and a clockwise vortex starts to form. In general, although the wake dynamics are similar in the three cases, differences are discernible at the wake as the plates deform with increasing Ca. A progressive weaker magnitude of the vortices is observed as the Cauchy number grows and the plates deform. Thus, the more streamlined shape of the trailing edge, defined by the closer location of rear plates edges, leads to a

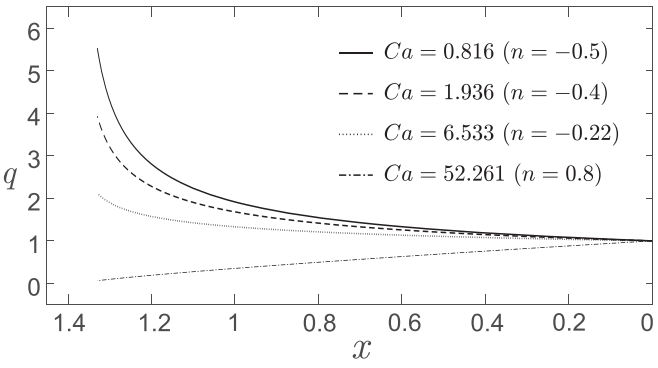

FIG. 8. Load distribution along the cantilever for different magnitudes of the loading exponent.

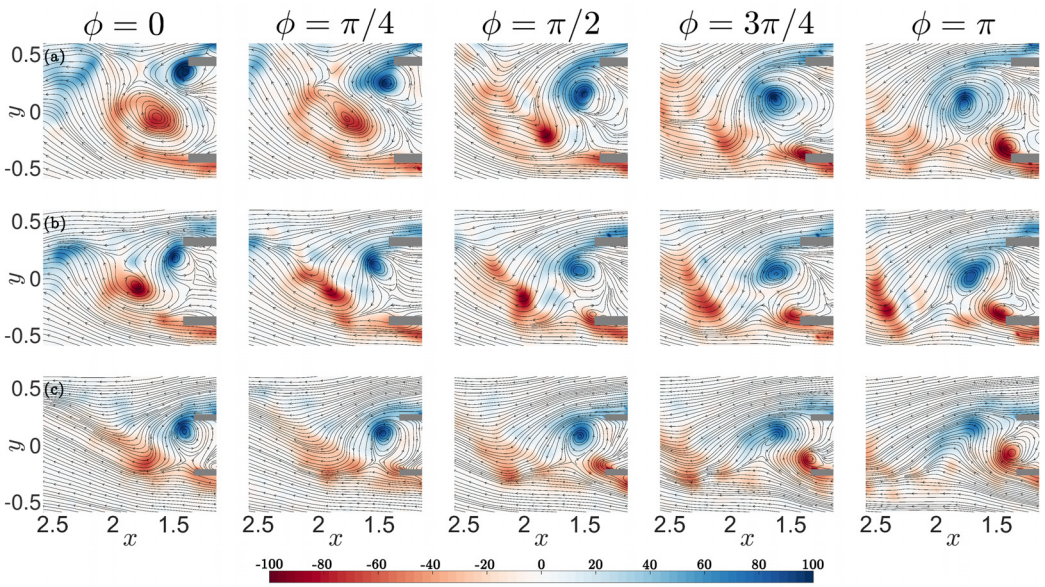

FIG. 9. Contours of instantaneous spanwise vorticity ω_z and corresponding streamlines for (a) $Ca = 1.936$, (b) $Ca = 6.533$, and (c) $Ca = 56.221$, describing a characteristic shedding cycle (note the flow is viewed from the bottom, i.e., negative z).

progressive smoother flow separation. The decrease on the vorticity magnitude, together with the limited size of the eddies at the near wake, which is restricted by the span between plates edges, may entail an important pressure recovery what would be the origin of the reduced drag coefficient observed for large values of *Ca*. Additionally, it is seen that the vorticity dissipates faster as it is advected downstream for increasing values of the Cauchy number, suggesting a faster recovery from the wake momentum deficit in the axial direction as the plates reconfigure. The overall weaker magnitude of vorticity observed in the near wake for increasing *Ca* may account as well for the reduction on the fluctuations amplitude of the drag coefficient shown in Fig. 4.

Furthermore, the plates reconfiguration occurring with increasing *Ca* decreases the distance between the shear layers, thus leading to a stronger interaction of vortices and an increase in the characteristic frequency. Moreover, the existence of a small step between the body base outer edge and the clamping grooves of the flexible moves the boundary layers away transversely from the plates for the stiffer cases, as seen, e.g., in Fig. 9(a). However, the strong deformation of the plates in Fig. 9(c) induces a closer attachment of the boundary layer on the cavity wall and a smoother flow separation. Such modifications may weaken the transverse pressure gradient toward the axis at the trailing edge, thus producing the decreasing loading distribution toward the tips obtained previously and sketched in Fig. 8.

The near wake modifications are further discussed with the help of the time-averaged contours of the axial velocity, $U_x(x, y)$, and the corresponding streamlines, depicted in Fig. 10, for $Ca = 0.817$, 1.936, 6.533, and 56.221. It is observed that the progressive mean reconfiguration of plates reduces the size of the recirculating bubble (note that there is a slight asymmetry in the recirculating bubble, which may be associated with the small number of cycles used in the averaging process). In particular, the deformation induces the flow to leave the cavity edges with a higher momentum toward the axis in the *y* coordinate (the concavity that develops the plate close to the rear edge may play an important role in that process, as illustrated in Lorite-Díez *et al.*[9]). As a result, the transverse height or bluffness decreases with increasing *Ca* (since it is defined by the span between the rear edges of the cavity), and the recirculating bubble is also shortened. The modification of the structure of the near wake also reduces the backflow velocity, $U_x < 0$ (as well as the vorticity magnitude as seen in Fig. 9).

In order to estimate the effect of the plates reconfiguration on the near wake, we compute the mean values of the recirculating bubble bluffness, H_r, and length, L_r, from the PIV measurements. The value of H_r is defined as the span between the midpoints of plates rear edge, while the length L_r is characterized as the maximum downstream location from the body base ($x = 0$) where $U_x \leq 0$. The trends with the Cauchy number of H_r and L_r are, respectively, depicted in Figs. 11(a) and 11(c). As observed, the variation of H_r with *Ca* is very similar to that of C_x shown in Fig. 4. In particular, due to its dependence on the evolution of the time-averaged angular deformation of plates [Fig. 6(a)], very small changes of H_r take place initially with increasing *Ca* for the stiffer cases, while a sudden decrease occurs for $Ca \geq 1.936$. Note that the reference value corresponding to the rigid case (#1 in Table I) is $H_{r,0} = 0.85$, while the minimum value of H_r for $Ca = 56.221$ is 0.476. On the other hand, the recirculating length L_r undergoes a monotonic decrease with increasing *Ca*, although it does feature neither any clear plateau at low values of *Ca* nor a linear trend in the logarithmic scale for larger *Ca*, as the bluffness H_r does.

The impact of the recirculating bubble size on the drag coefficient is next discussed with the help of Figs. 11(b) and 11(d), where the mean drag coefficient is, respectively, plotted vs H_r and H_r/L_r, which can be used as a good estimation of the near wake configuration, including the cavity length. The relation between separation length and base drag is a classical result for blunt-base bluff bodies. However,

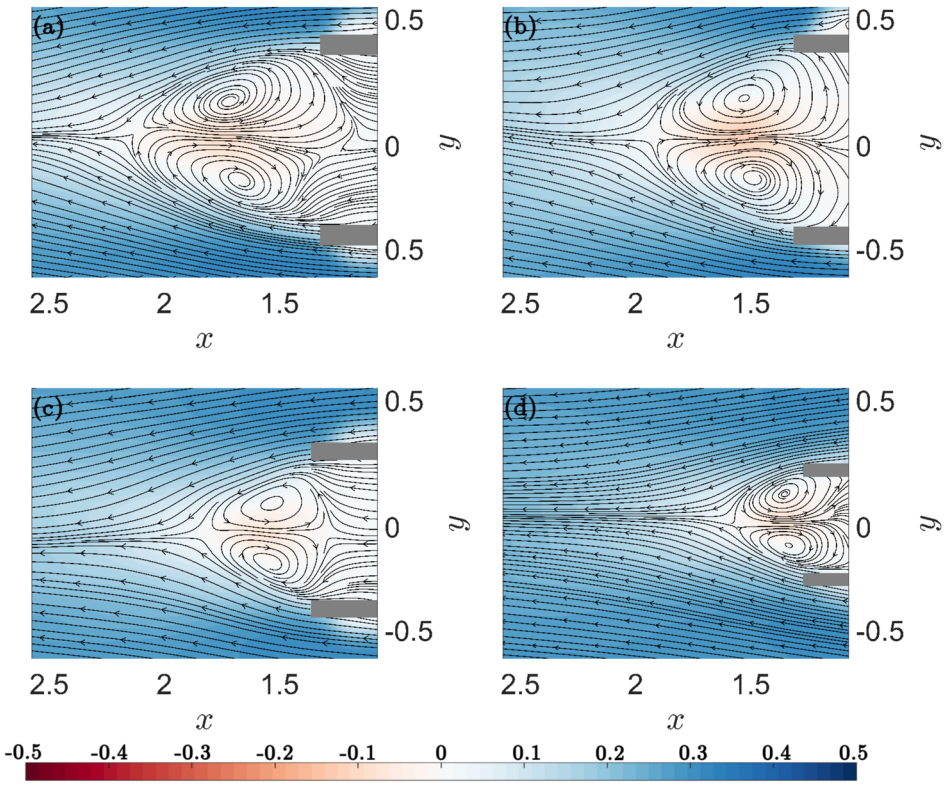

FIG. 10. Time-averaged contours of axial velocity $U_x(x, y)$ and corresponding streamlines for (a) $Ca = 0.817$, (b) 1.936, (c) 6.533, and (d) 56.221.

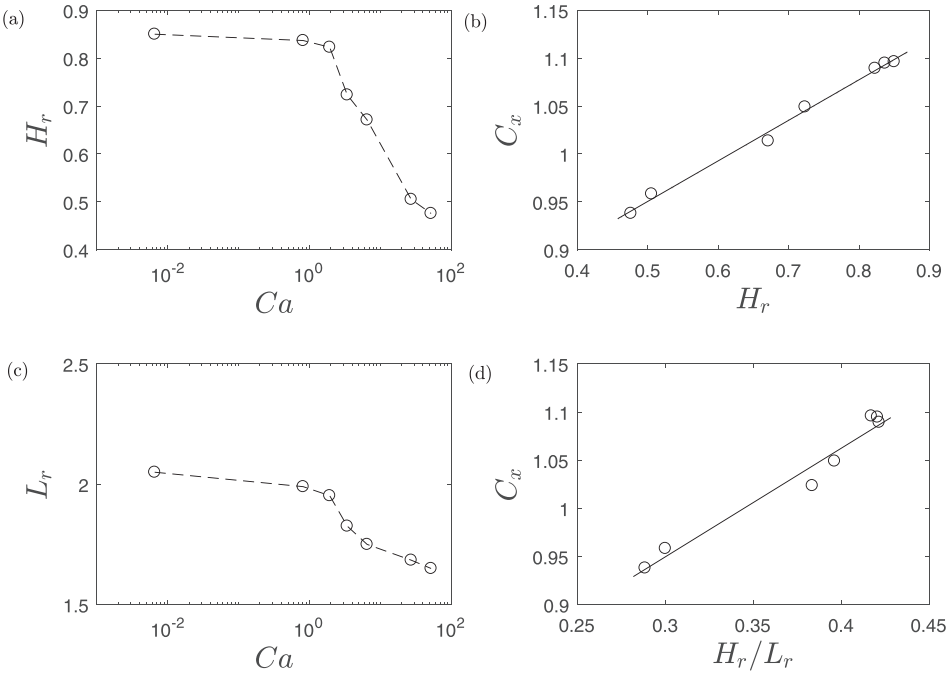

FIG. 11. Main time-averaged magnitudes of recirculating bubble and drag coefficient: (a) recirculating bubble bluffness H_r and (c) recirculating lengths L_r vs the Cauchy number Ca. Mean drag coefficient vs the (c) recirculating bubble bluffness H_r and (d) aspect ratio H_r/L_r. The solid lines in (b) and (d) represent, respectively, the fitting equations $C_x = 1.099 + 0.423(H_r - 0.85)$ and $C_x = 1.099 + 1.259(H_r/L_r - 0.420)$.

unlike the results reported in the literature for other wake control strategies, such as base blowing (see, e.g., Ref. 42), for which an increase in the recirculating length is related to a base drag recovery, in the present analysis, a direct relationship between recirculating length and drag can be inferred from results (not shown) because the recirculating bubble becomes smaller as Ca increases, as shown in Fig. 10. Therefore, it seems reasonable to think that the base pressure recovery is governed by the decrease in the bubble bluffness H_r and the near wake aspect ratio H_r/L_r. In fact, the bluffness reduction acts decreasing the flow curvature around the separation, as inferred from Fig. 10, what is consistent with lower values of base suction and force coefficients (as discussed by Wu[43] and Roshko[44] for bluff bodies wakes). Interestingly, a clear direct linear relationship exists between H_r and C_x. In particular, the affine relationship obtained through the data fitting reads

$$C_x = C_{x,0} + \alpha_1(H_r - H_{r,0}) = 1.099 + 0.423(H_r - 0.850), \quad (13)$$

with $H_{r,0} = 0.85$ and $C_{x,0} = 1.099$ being the bluffness and drag corresponding the reference case (#1 in Table I). Similarly, the data plotted in Fig. 11(d) fit reasonably well another direct relationship. Thus, it is shown that the mean drag coefficient C_x fairly varies linearly with the near wake aspect ratio H_r/L_r, following:

$$C_x = C_{x,0} + \alpha_2(H_r/L_r - H_{r,0}/L_{r,0}), \quad (14)$$

where $H_{r,0}/L_{r,0} = 0.420$ is the wake aspect ratio corresponding to the reference case, and $\alpha_2 = 1.259$. Thus, considering that for blunt-based bodies, it is accepted that variations of drag coefficient are proportional to variations of the base suction, defined as the negative pressure coefficient, i.e., $\Delta C_x \propto \Delta(-C_{pb})$, the relation (13) or (14) can be used to estimate the variations of base pressure induced by simply considering the transverse rear deformation of plates.

The previous result agrees well with the experimental observation of Bearman,[45] who showed for two-dimensional wakes that $-C_{pb}$ varies linearly with the reciprocal of the wake formation length, L_f, given by different splitter plates. These results were later generalized for wakes behind axisymmetric and symmetric plates of different bluffness by Humphries and Vincent.[46] Hence, although the downstream length L_r defined here is not necessarily the same as the lengths used in previous studies, as L_r also considers the cavity region, the general behavior is very similar. Unfortunately, the lack of pressure measurements at the base precluded us from further devise an argument on the precise role of the bubble shape and their influence on the inner stagnation flow region. However, a general empirical trend can be articulated from present and previous results on the dependence of base pressure or drag coefficients and the geometry of the near wake in bluff bodies.

V. CONCLUSIONS

The present experimental work has demonstrated the positive effect of the quasi-static reconfiguration of rear parallel plates on the drag coefficient of a slender blunt-based body. In general, increasing the flexibility of plates, within the range of Cauchy number $Ca = [0.006, 56.221]$, produces a progressive streamlining of the trailing edge that translates into important reductions of the mean drag coefficient and amplitude of fluctuations, with respective maximum values of nearly 14% and 10.5%. The limit on the potential reduction and the modification of the scaling law between drag force and velocity due to plates reconfiguration have been analyzed by means of the computation of an equivalent Vogel exponent. The minimum value has been found to be $\gamma = -0.131$ for $Ca = 3.422$, from where the exponent increases to seemingly reach an asymptotic value, as occurs in typical reconfiguration processes of flexible plates and filaments placed transversely to the flow stream, in spite of the different configuration of the fluid-structure interaction. Such trend for large Ca can be interpreted as a practical limit on the increasing drag reconfiguration, partly motivated by the beginning of stronger vibrations of plates.

The analysis of the deformation has revealed that the plates adapt to the flow mainly following shapes corresponding to primary normal modes of a deflected cantilever beam. However, a slight concavity develops toward the tip for large Cauchy numbers, on the account of the modifications on the flow loading that the increase in flexibility induces. Such progressive deformation translates into a weakening of the shedding process and a reduction of the recirculation bubble size characterized by an attenuated backflow. From such results, an affine direct relationship between recirculation bubble aspect ratio and drag coefficient has been finally proposed to unveil the connection between near wake modifications and hydrodynamic improvement provided by the trailing edge streamlining. Such empirical relation might be useful for the design of efficient passive control strategy in engineering systems concerning blunt bodies as, e.g., road transport or underwater vehicles.

The work reported here is in line with previous numerical studies developed by the same group. Considering the addition of the winglets and the large aspect ratio of the body used in our experiments, two-dimensional numerical simulations could be performed to complement this experimental study. The study could include the non-slip boundary condition at the sidewall of the tank to account for the blockage effect without having to apply any type of correction. The coupled dynamics between plates and flow could be resolved by means of Fluid Structure Interaction (FSI) simulations, carried out using nowadays extended approaches, e.g., OpenFOAM, which implements a partitioned, strongly coupled solution procedure. In that sense, considering the slow motion and progressive deformation of plates, the flexible plates may be modeled as a St. Venant-Kirchhoff elastic material, to properly account for finite strains and large deformations. Alternatively, the quasi-static reconfiguration of the plates would allow not only to perform FSI simulations but also a static study of the wake in the search for cavity shapes optimized for different Reynolds numbers, simplifying the computational time and resources needed. In any case, regardless of the undertaken analysis, such numerical work may help to identify limitations of the experimental study in the towing tank and extend it to other setup configurations.

ACKNOWLEDGMENTS

This work has been supported by the Spanish MICINN (Agencia Estatal de Investigación), Junta de Andalucía, Universidad de Jaén, and European Funds under Project Nos. DPI2017–89746-R and FEDER-UJA 1262764.

DATA AVAILABILITY

The data that support the findings of this study are available from the corresponding author upon reasonable request.

REFERENCES

[1]W. Hucho and G. Sovran, "Aerodynamics of road vehicles," Annu. Rev. Fluid Mech. **25**, 485–537 (1993).

[2]H. Choi, J. Lee, and H. Park, "Aerodynamics of heavy vehicles," Annu. Rev. Fluid Mech. **46**, 441–468 (2014).
[3]M. Gad-el-Hak, *Flow Control: Passive, Active, and Reactive Flow Management* (Cambridge University Press, 2000).
[4]F. Szodrai, "Quantitative analysis of drag reduction methods for blunt shaped automobiles," Appl. Sci. **10**, 4313 (2020).
[5]R. Verzicco, M. Fatica, G. Iaccarino, P. Moin, and B. Khalighi, "Large Eddy simulation of a road vehicle with drag-reduction devices," AIAA J. **40**, 2447–2455 (2002).
[6]D. R. Arcas and L. G. Redekopp, "Drag reduction of two-dimensional bodies by addition of boat tails," in *The Aerodynamics of Heavy Vehicles: Trucks, Buses, and Trains*, edited by R. McCallen, F. Browand, and J. Ross (Springer Berlin Heidelberg, Berlin, Heidelberg, 2004), pp. 237–248.
[7]A. Evrard, O. Cadot, V. Herbert, D. Ricot, R. Vigneron, and J. Délery, "Fluid force and symmetry breaking modes of a 3d bluff body with a base cavity," J. Fluids Struct. **61**, 99–114 (2016).
[8]M. Lorite-Díez, J. I. Jiménez-González, L. Pastur, O. Cadot, and C. Martínez-Bazán, "Drag reduction on a three-dimensional blunt body with different rear cavities under cross-wind conditions," J. Wind Eng. Ind. Aerodyn. **200**, 104145 (2020).
[9]M. Lorite-Díez, J. I. Jiménez-González, C. Gutiérrez-Montes, and C. Martínez-Bazán, "Drag reduction of slender blunt-based bodies using optimized rear cavities," J. Fluids Struct. **74**, 158–177 (2017).
[10]R. Abdi, N. Rezazadeh, and M. Abdi, "Investigation of passive oscillations of flexible splitter plates attached to a circular cylinder," J. Fluids Struct. **84**, 302–317 (2019).
[11]J. Deng, X. Mao, and F. Xie, "Dynamics of two-dimensional flow around a circular cylinder with flexible filaments attached," Phys. Rev. E **100**, 053107 (2019).
[12]C. García-Baena, J. I. Jiménez-González, C. Gutiérrez-Montes, and C. Martínez-Bazán, "Numerical analysis of the flow-induced vibrations in the laminar wake behind a blunt body with rear flexible cavities," J. Fluids Struct. **100**, 103194 (2021).
[13]F. Fish and G. Lauder, "Passive and active flow control by swimming fishes and mammals," Annu. Rev. Fluid Mech. **38**, 193–224 (2006).
[14]H. Choi, H. Park, W. Sagong, and S.-I. Lee, "Biomimetic flow control based on morphological features of living creatures," Phys. Fluids **24**, 121302 (2012).
[15]N. Mazellier, A. Feuvrier, and A. Kourta, "Biomimetic bluff body drag reduction by self-adaptive porous flaps," C. R. Mec. **340**, 81–94 (2012), biomimetic flow control.
[16]D. Kim, H. Lee, W. Yi, and H. Choi, "A bio-inspired device for drag reduction on a three-dimensional model vehicle," Bioinspiration Biomimetics **11**, 026004 (2016).
[17]K. R. Sharma and S. Dutta, "Flow control over a square cylinder using attached rigid and flexible splitter plate at intermediate flow regime," Phys. Fluids **32**, 014104 (2020).
[18]D. L. Harder, O. Speck, C. L. Hurd, and T. Speck, "Reconfiguration as a prerequisite for survival in highly unstable flow-dominated habitats," J. Plant Growth Regul. **23**, 98–107 (2004).
[19]X. Zhang and H. Nepf, "Flow-induced reconfiguration of aquatic plants, including the impact of leaf sheltering," Limnol. Oceanogr. **65**, 2697–2712 (2020).
[20]S. Vogel, "Drag and flexibility in sessile organisms," Am. Zool. **24**, 37–44 (1984).
[21]S. Vogel, "Drag and reconfiguration of broad leaves in high winds," J. Exp. Botany **40**, 941–948 (1989).
[22]S. Alben, M. Shelley, and J. Zhang, "Drag reduction through self-similar bending of a flexible body," Nature **420**, 479 (2002).
[23]F. Gosselin, E. De Langre, and B. A. Machado-Almeida, "Drag reduction of flexible plates by reconfiguration," J. Fluid Mech. **650**, 319–341 (2010).
[24]F. P. Gosselin and E. de Langre, "Drag reduction by reconfiguration of a poroelastic system," J. Fluids Struct. **27**, 1111– 1123 (2011).
[25]M. J. Shelley and J. Zhang, "Flapping and bending bodies interacting with fluid flows," Annu. Rev. Fluid Mech. **43**, 449–465 (2011).
[26]E. de Langre, A. Gutierrez, and J. Cossé, "On the scaling of drag reduction by reconfiguration in plants," C. R. Mec. **340**, 35–40 (2012).
[27]A. Bhati, R. Sawanni, K. Kulkarni, and R. Bhardwaj, "Role of skin friction drag during flow-induced reconfiguration of a flexible thin plate," J. Fluids Struct. **77**, 134–150 (2018).
[28]Y. Jin, J.-T. Kim, S. Cheng, O. Barry, and L. P. Chamorro, "On the distinct drag, reconfiguration and wake of perforated structures," J. Fluid Mech. **890**, A1 (2020).
[29]M. Lorite-Díez, J. I. Jiménez-González, C. Gutiérrez-Montes, and C. Martínez-Bazán, "Effects of rear cavities on the wake behind an accelerating d-shaped bluff body," Phys. Fluids **30**, 044103 (2018).
[30]S. S. Rao, *Mechanical Vibrations*, 5th ed. (Prentice-Hall, 2011).
[31]F. Huera-Huarte and J. I. Jiménez-González, "Effect of diameter ratio on the flow-induced vibrations of two rigidly coupled circular cylinders in tandem," J. Fluids Struct. **89**, 96–107 (2019).
[32]W. Thielicke and E. Stamhuis, "PIVlab-towards user-friendly, affordable and accurate digital particle image velocimetry in MATLAB," J. Open Res. Software **2**(1), e30 (2014).
[33]H. W. Coleman and W. G. Steele, *Experimentation, Validation, and Uncertainty Analysis for Engineers*, 3rd ed. (John Wiley and Sons, Hoboken, NJ, 2009).
[34]A. Sciacchitano, "Uncertainty quantification in particle image velocimetry," Meas. Sci. Technol. **30**, 092001 (2019).
[35]R. Adrian, "Multi-point optical measurements of simultaneous vectors in unsteady flow-a review," Int. J. Heat Fluid Flow **7**, 127–145 (1986).
[36]J. N. Fernando and D. E. Rival, "On vortex evolution in the wake of axisymmetric and non-axisymmetric low-aspect-ratio accelerating plates," Phys. Fluids **28**, 017102 (2016).
[37]S. Satheesh and F. J. Huera-Huarte, "Effect of free surface on a flat plate translating normal to the flow," Ocean Eng. **171**, 458–468 (2019).
[38]S. Alben, M. Shelley, and J. Zhang, "How flexibility induces streamlining in a two-dimensional flow," Phys. Fluids **16**, 1694–1713 (2004).
[39]T. Leclercq and E. de Langre, "Drag reduction by elastic reconfiguration of non-uniform beams in non-uniform flows," J. Fluids Struct. **60**, 114–129 (2016).
[40]S. Satheesh and F. J. Huera-Huarte, "On the drag reconfiguration of plates near the free surface," Phys. Fluids **31**, 067106 (2019).
[41]S. Timoshenko, *Strength of Materials* (D. van Nostrand Company, Inc., 1930).
[42]M. Lorite-Díez, J. I. Jiménez-González, L. Pastur, C. Martínez-Bazán, and O. Cadot, "Experimental analysis of the effect of local base blowing on three-dimensional wake modes," J. Fluid Mech. **883**, A53 (2020).
[43]T. Y. T. Wu, "Cavity and wake flows," Annu. Rev. Fluid Mech. **4**, 243–284 (1972).
[44]A. Roshko, "Perspectives on bluff body aerodynamics," J. Wind Eng. Ind. Aerodyn. **49**, 79–100 (1993).
[45]P. W. Bearman, "Investigation of the flow behind a two-dimensional model with a blunt trailing edge and fitted with splitter plates," J. Fluid Mech. **21**, 241–255 (1965).
[46]W. Humphries and J. Vincent, "Near wake properties of axisymmetric bluff body flows," Appl. Sci. Res. **32**, 649–669 (1976).